

## Polarization angle scanning for wide-band millimeter-wave direct detection

WANG He-Yao<sup>1,2</sup>, ZHAO Zi-Ran<sup>1,2\*</sup>, QIAO Ling-Bo<sup>1,2</sup>, GUO Da-Lu<sup>1,2</sup>

- (1. Department of Engineering Physics, Tsinghua University, Beijing 100084, China;  
2. National Engineering Research Center of Dangerous Articles and Explosives Detection Technologies, Beijing 100084, China)

**Abstract:** Millimeter-wave (MMW) technology has been widely utilized in human security screening applications due to its superior penetration capabilities through clothing and safety for human exposure. However, existing methods largely rely on fixed polarization modes, neglecting the potential insights from variations in target echoes with respect to incident polarization. This study provides a theoretical analysis of the cross-polarization echo power as a function of the incident polarization angle under linear polarization conditions. Additionally, based on the transmission characteristics of multi-layer medium, we extend the depth spectrum model employed in direct detection to accommodate scenarios involving multi-layered structures. Building on this foundation, by obtaining multiple depth spectra through polarization angle scanning, we propose the Polarization Angle-Depth Matrix to characterize targets across both the polarization angle and depth dimensions in direct detection. Simulations and experimental validations confirm its accuracy and practical value in detecting concealed weapons in human security screening scenarios.

**Key words:** millimeter-wave, cross-polarization, polarization angle scanning, concealed weapon, direct detection

## 用于宽带毫米波直接探测的极化角度扫描方法

王贺尧<sup>1,2</sup>, 赵自然<sup>1,2\*</sup>, 乔灵博<sup>1,2</sup>, 郭大路<sup>1,2</sup>

- (1. 清华大学工程物理系, 北京 100084;  
2. 危爆物品探测技术国家工程研究中心, 北京 100084)

**摘要:**毫米波技术因其对衣物的良好穿透能力和对人体的辐射安全性,在人体安检领域得到了广泛应用。然而,现有技术多采用固定极化模式,忽视了目标回波随入射极化的变化中可能蕴含的潜在信息。本文从理论上分析了线极化条件下目标交叉极化回波功率随入射极化角度的变化规律,并基于多层介质的传输特性将直接探测中的深度谱模型拓展到多层介质情况。在此基础上,通过入射极化角度扫描获取多个深度谱,提出了极化角度-深度矩阵,用于在直接探测中对目标极化角度和深度两个维度上的特性进行表征。仿真和实验验证了上述分析的准确性以及在人体安检场景隐藏武器探测中的实用价值。

**关键词:**毫米波;交叉极化;极化角度扫描;隐藏武器;直接探测

中图分类号: TP391.4

文献标识码: A

### Introduction

Millimeter-wave (MMW) technology offers superior penetration through clothing while ensuring safe radiation levels, making it an excellent choice for concealed weapon detection. In recent years, MMW technology has

been extensively studied and applied in human security screening<sup>[1]</sup>. The polarization characteristics of electromagnetic waves contain valuable information about the structure and material properties of targets. Multi-polarization detection, which introduces additional dimensions of information<sup>[2-3]</sup>, has become increasingly central

Received date: 2025-03-21, accepted date: 2025-05-12

收稿日期: 2025-03-21, 录用日期: 2025-05-12

Foundation items: Supported by the National Key Research and Development Program of China (2023YFF0715000)

Biography: WANG He-Yao (1997—), male, Hebei, Ph. D. student. Research interests involve millimeter wave detection and imaging technology. E-mail: wangheya20@mails.tsinghua.edu.cn

\* Corresponding author: E-mail: zhaozr@tsinghua.edu.cn

in improving detection accuracy. Furthermore, under a single polarization condition, different polarization directions result in variations in the information acquired<sup>[4-5]</sup>, making multi-polarization detection an increasingly important research focus.

In passive MMW detection, two-dimensional Stokes vector images obtained through fully polarized radar have been employed for analyzing target clustering characteristics<sup>[6]</sup>. Image quality can be improved by averaging images acquired from three different polarization directions<sup>[7]</sup>. Additionally, by collecting images under different linear polarization directions and calculating specific parameters, previous studies have explored various applications, including imaging quality enhancement<sup>[8]</sup>, target contour extraction<sup>[9]</sup>, and contrast improvement<sup>[10-11]</sup>.

In active MMW detection, dual-polarization imaging systems have been integrated into holographic imaging systems for human security screening, effectively improving detection accuracy<sup>[12]</sup>. Since concealed objects exhibit significantly different polarization characteristics compared to the human body, their co-polarization and cross-polarization echoes vary accordingly. By extracting co-polarization and cross-polarization echo information and computing polarization-related parameters such as the polarization ratio, concealed objects can be identified<sup>[13-17]</sup>. Furthermore, by performing H- $\alpha$  decomposition on the full-polarization information of a target, material classification can be achieved based on its location in the H- $\alpha$  plane<sup>[18]</sup>. Several studies have further explored the differences between human bodies and weapons in co-polarization and cross-polarization images by comparing four-channel images under horizontal and vertical polarizations<sup>[19-22]</sup>.

However, most of the mentioned studies rely on fixed polarization modes (e. g., horizontal, vertical, or  $\pm 45^\circ$ ) and have not thoroughly investigated the variations in target echoes with respect to the incident polarization angle. To address this limitation, this study analyzes the variation in cross-polarization echo power as a function of the incident polarization angle and derives its theoretical expression. The depth spectrum utilized in millimeter-wave (MMW) direct detection is based on the wide-band power information and represents the distribution of the target along the depth direction<sup>[16]</sup>. Based on the transmission characteristics of multi-layer medium, we extend the depth spectrum model to better align with real-world scenarios. Building upon this, we examine the differences in cross-polarization responses and depth distribution between human surfaces and concealed weapons. By scanning the incident polarization angle and obtaining multiple depth spectra, we introduce the Polarization Angle-Depth Matrix to characterize the features in polarization response and depth distribution. Through both simulations and experiments, the proposed analysis is validated, demonstrating its potential application value in human security screening for concealed weapon detection. By employing direct detection, which means only capturing power information while omitting phase acquisition, the proposed method eliminates the mixing modules re-

quired in conventional coherent detection systems. This approach consequently reduces both system complexity and implementation costs in practical applications.

The remainder of this paper is structured as follows: Section 1 investigates the variation in cross-polarization echo power with incident polarization angle and explores the depth-wise distribution characteristics of multi-layer targets, providing corresponding theoretical formulations. The differences between human bodies and weapons in these two dimensions are further analyzed, and the Polarization Angle-Depth Matrix is introduced for feature representation. Section 2 presents the simulation and experimental results, verifying the theoretical analysis and demonstrating the potential application value of the proposed matrix in human security screening. Section 3 concludes the paper with a summary of key findings.

## 1 Theory and characteristic analysis of the Polarization Angle-Depth Matrix

### 1.1 Variation of cross-polarization power with incident linear polarization angle

Previous study<sup>[23]</sup> has shown that the human body surface can be approximately modeled as a planar or cylindrical surface. When linearly polarized waves are incident on the human body surface, the scattered echoes predominantly exhibit co-polarized components, while cross-polarized components are generally weak. However, for weapons, due to their relatively complex structures, the cross-polarized components in the scattered echoes are significantly stronger. Based on this observation, individuals carrying concealed weapons exhibit notable differences in cross-polarized echo power compared to ordinary individuals. Meanwhile, due to the differences in the polarization scattering matrices of weapons and the human body surface, the variation of cross-polarization echo power with incident polarization angle also differs. This section will theoretically derive this variation pattern.

In the horizontal-vertical coordinate system h - v, the polarization scattering matrix of a target at a given incident angle is defined as  $S = \begin{bmatrix} s_{hh} & s_{hv} \\ s_{vh} & s_{vv} \end{bmatrix}$ , where the incident wave is expressed as  $E_T = \begin{bmatrix} E_{Th} \\ E_{Tv} \end{bmatrix} = \begin{bmatrix} \cos \eta \\ \sin \eta \end{bmatrix}$ , here  $\eta$  is the polarization angle. The scattered echo can then be written as:

$$E_R = SE_T = \begin{bmatrix} s_{hh} \cos \eta + s_{hv} \sin \eta \\ s_{vh} \cos \eta + s_{vv} \sin \eta \end{bmatrix} = \begin{bmatrix} E_{Rh} \\ E_{Rv} \end{bmatrix}. \quad (1)$$

To analyze the cross-polarization, a new orthogonal polarization basis, denoted as h' - v', is introduced. Here, h' represents the polarization direction of the incident wave. This basis is equivalent to rotating the original h - v coordinate system by an angle  $\eta$  about the origin. By transforming  $E_R$  using the rotation matrix  $R = \begin{bmatrix} \cos \eta & \sin \eta \\ -\sin \eta & \cos \eta \end{bmatrix}$ , the cross-polarization component can be obtained as  $E'_{Rv} = E_{Rv} \cos \eta - E_{Rh} \sin \eta$ . The cross-po-

larization power is then defined as:

$$P_{\text{cross}}(\eta) = \|E'_{\text{Rv}}\|^2 = \|E_{\text{Rh}}\|^2 \sin^2 \eta + \|E_{\text{Rv}}\|^2 \cos^2 \eta - (E_{\text{Rv}}^* E_{\text{Rh}} + E_{\text{Rh}}^* E_{\text{Rv}}) \sin \eta \cos \eta \quad (2)$$

Define coefficients as:

$$\begin{aligned} a_1 &= |s_{\text{hv}}|^2 \\ a_2 &= 2\text{Re}\{s_{\text{hv}}^*(s_{\text{hh}} - s_{\text{vv}})\} \\ a_3 &= |s_{\text{hh}}|^2 + |s_{\text{vv}}|^2 - 2(\text{Re}\{s_{\text{hv}}^* s_{\text{vh}}\} + \text{Re}\{s_{\text{hh}}^* s_{\text{vv}}\}), \\ a_4 &= 2\text{Re}\{s_{\text{vh}}^*(s_{\text{vv}} - s_{\text{hh}})\} \\ a_5 &= |s_{\text{vh}}|^2 \end{aligned} \quad (3)$$

and

$$\begin{aligned} A_1 &= \frac{1}{4} \sqrt{4(a_5 - a_1)^2 + (a_2 + a_4)^2} \\ B_1 &= -\arctan\left(\frac{a_2 + a_4}{2(a_5 - a_1)}\right) \\ A_2 &= \frac{1}{8} \sqrt{(a_1 + a_5 - a_3)^2 + (a_4 - a_2)^2} \\ B_2 &= -\arctan\left(\frac{a_4 - a_2}{a_1 + a_5 - a_3}\right) \\ C &= \frac{1}{8} (3a_1 + 3a_5 + a_3) \end{aligned} \quad (4)$$

then we can obtain a further simplified form:

$$P_{\text{cross}}(\eta) = A_1 \cos(2\eta + B_1) + A_2 \cos(4\eta + B_2) + C \quad (5)$$

According to Eq. (4), the following properties can be derived:

1) The variation of the target's cross-polarization power with incident polarization angle is expressed as the sum of two cosine functions with periodicities of  $\pi$  and  $\pi/2$ , respectively. The amplitudes and phase shifts of these cosine functions are determined by the polarization scattering matrix of the target.

2) If the target is rotated by an angle  $\theta$  around the incident direction (i. e., the  $z$ -axis), it is equivalent to keeping the target fixed while rotating the incident wave polarization angle by  $-\theta$ . This results in a translation of Eq. (4), leading to the following equivalent expression:

$$P_{\text{cross}}(\eta) = A_1 \cos(2(\eta + \theta) + B_1) + A_2 \cos(4(\eta + \theta) + B_2) + C \quad (6)$$

For most common weapons, such as metallic handguns, the co-polarization components of the polarization scattering matrix are typically 1-2 orders of magnitude higher than the cross-polarization components, i. e.,  $s_{\text{hh}}, s_{\text{vv}} \gg s_{\text{hv}}, s_{\text{vh}}$ . Under this condition, the amplitude coefficients in Eq. (4) satisfy  $A_2 \gg A_1$ . Consequently, the  $A_2 \cos(4\eta + B_2)$  term in Eq. (4) becomes the dominant component, while the  $A_1 \cos(2\eta + B_1)$  term introduces only minor amplitude and phase modulations.

## 1.2 Depth spectrum theory of the multi-layer medium

For scenarios where dangerous items are carried on

the human body, the situation can be equivalently modeled as a multi-layered medium placed in front of a semi-infinite medium (the human body), as illustrated in Fig. 1. Stuart W. Harmer et al. provided a theoretical expression for a multi-scattering point model, which bore similarity to the multi-layered medium. By utilizing only the echo power information, they derived a mathematical expression that characterized the separations between the scattering points, referred to as the depth spectrum<sup>[16]</sup>:

$$\begin{aligned} s'(\tau) &= \sum_{u=1}^{n-1} \sum_{i=1}^{n-1} F^{-1}\{a_i(f) a_u^*(f)\} \otimes \delta\left(\tau - \frac{2}{c}(z_i - z_u)\right) \\ &= \sum_{i=1}^{n-1} F^{-1}\{|a_i(f)|^2\} \delta(\tau) \\ &+ \sum_{u=2}^{n-1} \sum_{i=1}^{n-u} F^{-1}\{a_i^*(f) a_{i+u-1}(f)\} \delta\left(\tau - \frac{2}{c}(z_{i+u-1} - z_{i+1})\right) \end{aligned} \quad (7)$$

where  $a_i$  represents the scattering strength,  $z_i$  denotes the distance between scattering point  $i$  and the transceiver antenna,  $F^{-1}$  represents the inverse Fourier transform and  $\otimes$  represents the convolution operator.

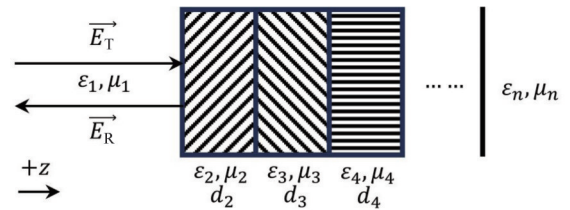


Fig. 1 Plane wave incidence on a multi-layer medium  
图1 平面波入射多层介质

However, Eq. (7) cannot intuitively represent the characteristics of the depth spectrum in a multi-layer medium model. This limitation arises because Eq. (7) is based on the assumption that scattering points are independent of each other. In multi-layer medium, the intensity of the incident wave at each interface is influenced by the transmission and attenuation effects of the preceding layers. As a result, the scattering coefficient  $a_i$  at one specific interface inherently contains an exponential attenuation term related to the material properties and thickness of all preceding layers. After performing the inverse Fourier transform, this attenuation term also exhibits the form of a  $\delta$ -function, which merges with the original terms in Eq. (7). Consequently, in multi-layer medium, the positions of the  $\delta$ -functions in the depth spectrum no longer directly correspond to the actual physical distances between interfaces but rather to the optical depth.

S. W. Harmer et al. theoretically derived the depth spectrum form for a single wax layer placed on the surface of the human body in Ref. [15]. This paper further derives the depth spectrum form for multi-layer mediums.

Assuming that a uniform plane wave is normally incident on the surface of a multi-layer isotropic medium. Under the assumption of single reflection at each interface, the equivalent reflection coefficient of the entire

medium structure can be expressed as:

$$R = Q_1 + \sum_{i=2}^{n-1} Q_i \exp\left(-j2 \sum_{q=2}^i \beta_q d_q\right) \quad (8)$$

where  $Q_i = \prod_{p=1}^{i-1} r_{ii+1} t_{pp+1} t_{p+1p} \exp(-2 \sum_{q=2}^i \alpha_q d_q)$  for  $i \geq 2$ , and  $Q_1 = r_{12}$ . Here  $r_{ii+1}$  represents the reflection coefficient of the incident wave in the +z-direction at the interface between medium  $i$  and  $i+1$ . Similarly,  $t_{i+1i}$  represents the transmission coefficient of the incident wave in the +z-direction at the same interface. The complex wavenumber in medium  $i$  is defined as  $\kappa_i = \frac{2\pi f}{c} \sqrt{\varepsilon_i \mu_i} = \beta_i - j\alpha_i$ , where  $\alpha_i$  is the attenuation factor, and  $\beta_i$  is the phase factor.

Assuming that within the frequency band of interest  $\varepsilon_i$  is constant,  $\alpha_i$  is negligible (i. e.,  $\varepsilon_i \approx \text{Re}\{\varepsilon_i\}$ ), and  $\mu_i = 1$ , the phase factor becomes  $\beta_i = \frac{2\pi f}{c} \sqrt{\varepsilon_i}$ . Under these conditions, the reflection coefficient simplifies to  $r_{ii+1} = \frac{\sqrt{\varepsilon_i} - \sqrt{\varepsilon_{i+1}}}{\sqrt{\varepsilon_i} + \sqrt{\varepsilon_{i+1}}}$ , which is also constant.

In a monostatic transceiver configuration, the frequency-domain representation of the target's scattered echo can be expressed as  $S(f) = A(f)R(f)\exp(-j\frac{4\pi f}{c}z_0)$ , where  $A(f)$  is the gain coefficient determined by the radiation patterns of the transmitting and receiving antennas. This can be normalized using strong scatterers such as metallic plates. Here,  $z_0$  denotes the distance between the target and the transceiver system. The normalized time-domain signal can be expressed as  $s_n(t) = F^{-1}[S(f)] = F^{-1}[R(f)] \otimes \delta\left(t - \frac{2z_0}{c}\right)$ .

Using Eq. (8), we can derive:

$$F^{-1}[R(f)] = Q_1 + \sum_{i=2}^{n-1} Q_i \delta\left(t - \frac{2 \sum_{q=2}^i \sqrt{\varepsilon_q} d_q}{c}\right) \quad (9)$$

Substituting Eq. (9) into the time-domain signal expression, we obtain:

$$s_n(t) = Q_1 \delta\left(t - \frac{2z_0}{c}\right) + \sum_{i=2}^{n-1} Q_i \delta\left(t - \frac{2\left(z_0 + \sum_{q=2}^i \sqrt{\varepsilon_q} d_q\right)}{c}\right) \quad (10)$$

At the receiver, the measured broadband power signal is  $|S(f)|^2$ . Performing the inverse Fourier transform on it is equivalent to computing the autocorrelation of the time-domain echo signal (ignoring constant scaling factors of the transform):

$$s'(\tau) = F^{-1}\left[|S(f)|^2\right] = s_n^*(-t) \otimes s_n(t) \quad (11)$$

By combining Eq. (10) and Eq. (11), and taking incident polarization angle  $\eta$  into account, we arrive at (negative time-axis terms are discarded):

$$s'_X(\tau, \eta) = \sum_{i=1}^{n-1} |Q_{X_i}(\eta)|^2 \delta\left(\tau - \frac{2 \sum_{v=i+1}^{n-1} \sqrt{\varepsilon_v} d_v}{c}\right) + \sum_{u=2}^{n-1} \sum_{i=1}^{n-u} Q_{X_i}^*(\eta) Q_{X_{i+u-1}}(\eta) \delta\left(\tau - \frac{2 \sum_{v=i+1}^{i+u-1} \sqrt{\varepsilon_v} d_v}{c}\right) \quad (12)$$

Here, the subscript  $X$  denotes the cross-polarization. Compared to Eq. (7), the  $\delta$ -function positions in the depth spectrum of the multi-layer medium, as expressed in Eq. (12), correspond to  $\sqrt{\varepsilon_q} d_q$ , which is referred to as the optical thickness, and their amplitudes are determined by the reflection and transmission coefficients of each layer.

### 1.3 Characteristics of the Polarization Angle-Depth Matrix

Based on the previous analysis, to characterize the differences between the human body surface and weapons in both polarization response and depth dimensions, we propose the Polarization Angle-Depth Matrix as a data representation. By discretizing  $\eta$  and  $\tau$ , Eq. (12) can be expressed in matrix form as:

$$U_X = \begin{bmatrix} s'_X(\tau_1, \eta_1) & \cdots & s'_X(\tau_M, \eta_1) \\ \vdots & \ddots & \vdots \\ s'_X(\tau_1, \eta_N) & \cdots & s'_X(\tau_M, \eta_N) \end{bmatrix} \quad (13)$$

Equation (13) is referred to as the Polarization Angle-Depth Matrix of the target. Further analysis will be conducted on the two-dimensional characteristics of Eq. (13).

1) The column dimension of  $U_X$  represents the incident polarization angle. The first column can be expressed as:

$$s'_X(0, \eta) = \sum_{i=1}^{n-1} |Q_{X_i}(\eta)|^2 \delta(0) \quad (14)$$

According to the analysis in Section 1, Eq. (14) follows the variation pattern described in Eq. (5) with respect to the incident polarization angle. For different targets, the characteristics of their polarization scattering matrices result in significant differences in the amplitude and phase of the cosine functions.

For the human body surface, since  $s_{\text{hv}}$  and  $s_{\text{vh}}$  are approximately zero, the cross-polarization reflection coefficient is very small, leading to minimal variation in  $s'_X(0, \eta)$  with respect to  $\eta$ . This implies that the amplitude terms  $A_1$  and  $A_2$  in Eq. (5) are small. Furthermore, for a standing human body, the rotational angle around the incident direction remains fixed, leading to a constant phase in Eq. (5), i. e.,  $B_1$  and  $B_2$  remain nearly unchanged.

For weapons, the values of  $s_{\text{hv}}$  and  $s_{\text{vh}}$  increase significantly, leading to a much higher overall cross-polarization power compared to the human body surface. As a result, the amplitude of the cosine functions in Eq. (5) increases notably. Additionally, due to variations in the rotational angle of the weapon around the incident direction, the phase terms in Eq. (5) may differ from those of

the human body.

2) The rows of  $U_x$  represent the depth dimension. Denoting the depth spectrum at a specific incident polarization angle  $\eta_0$ , it can be rewritten as Eq. (12) of  $s'_x(\tau, \eta_0)$ .

For the human body surface, since there is no multi-layer structure, the Dirac delta sequence in Eq. (12) contains only the first term, meaning that there is a single peak at  $\tau = 0$ .

For weapons, which can be equivalently modeled as a multi-layer structure, multiple peaks corresponding to the second term in Eq. (12) will appear in addition to the first peak. Furthermore, due to the increased cross-polarization reflection coefficient, the peak at  $\tau = 0$  is significantly higher than that of the human body surface.

Based on the above analysis, the Polarization Angle-Depth Matrix exhibits distinct characteristics along both its column and row dimensions. The human body surface shows a smooth polarization response with a single peak in the depth spectrum. Weapons, on the other hand, exhibit a higher polarization response amplitude and contain multiple peaks in the depth spectrum. These characteristics provide a reliable basis for the effective detection of concealed weapons.

## 2 Simulations and experiments

### 2.1 Simulation results

To validate the effectiveness of the proposed analysis, we conducted a simulation using FEKO software. First, we verified the correctness of Eqs. (4) and (5). We utilized a target composed of a combination of a rectangular dihedral reflector and a flat plate, as shown in Fig. 2. During the simulation, the dihedral reflector was rotated by certain angles around both the  $z$ -axis and the  $y$ -axis. A uniform plane wave was used as the incident wave to obtain the polarization scattering matrix  $S$  of the target. By scanning the incident polarization angle, we obtained multiple  $(P_{\text{cross}}, \eta)$  data pairs. These data pairs were subsequently used for curve fitting. The curve fitting results obtained from simulated power values in FEKO software were compared with the theoretical calculations based on the polarization scattering matrix, as

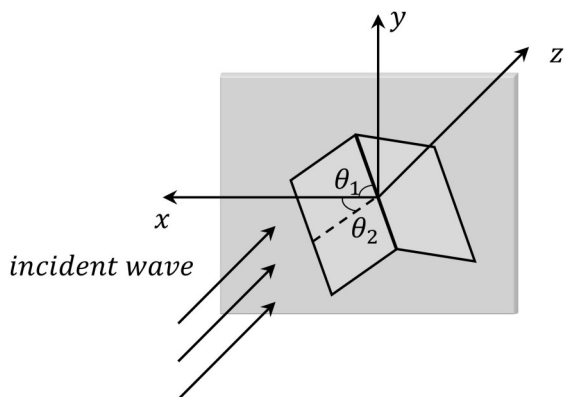


Fig. 2 Schematic of the simulation scenario (dihedral reflector and flat plate)

图2 仿真场景示意图(二面角反射器和平板)

shown in Fig. 3.

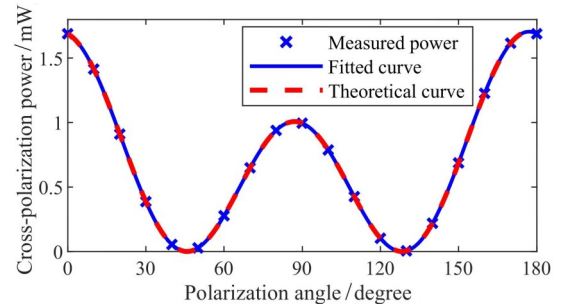


Fig. 3 Curve fitting and theoretical calculation results ( $\theta_1 = -50^\circ, \theta_2 = 20^\circ$ )

图3 曲线拟合与理论计算结果( $\theta_1=-50^\circ, \theta_2=20^\circ$ )

Figure 3 demonstrates that the cross-polarization power curve obtained from theoretical calculations aligns closely with the results of cosine fitting based on the collected power data points. This confirms the validity of Eqs. (4) and (5).

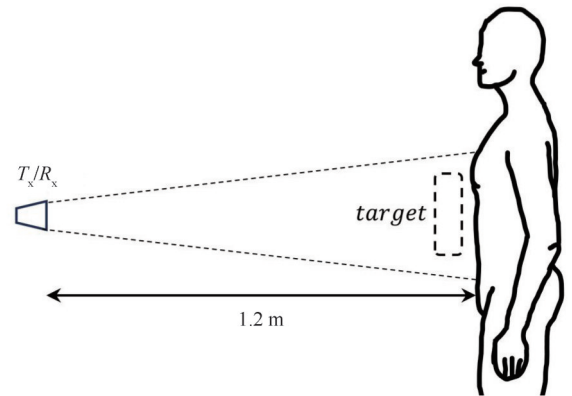


Fig. 4 Schematic of the simulation scenario

图4 仿真场景示意图

Next, we conducted a simulation analysis of the Polarization Angle-Depth Matrix. In FEKO software, we modeled two metallic grenades, a metallic handgun, and a human body, and performed simulations where the grenades and handgun were placed on the human body surface. These cases were compared with the scenario of a standalone human body, as illustrated in Fig. 4. In the simulation, the frequency range was configured from 75 GHz to 110 GHz with a 1 GHz sampling interval, where the signal was generated through a point-by-point sweep of discrete frequency points. The polarization angle range was set from  $0^\circ$  to  $180^\circ$ , with a sampling interval of  $10^\circ$ . The simulated Polarization Angle-Depth Matrix obtained from these scenarios is shown in Fig. 5.

As shown in Fig. 4, the fitting curve following the principle of Eq. (5) maintains good agreement with simulated power points in practical scenario modeling, verifying the applicability of Eq. (5) in real-world conditions. Figure 5 demonstrates significant differences in the Polarization Angle-Depth Matrix between individuals

carrying concealed weapons and normal individuals.

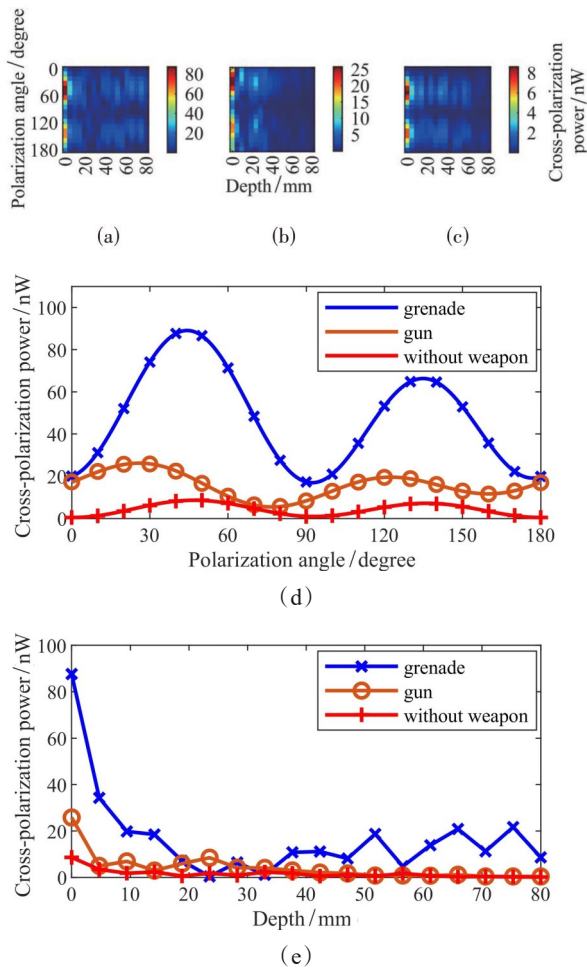


Fig. 5 Simulation results of the Polarization Angle-Depth Matrix in three scenarios: (a) carrying grenade model; (b) carrying handgun model; (c) without weapons; (d) first column of the Polarization Angle-Depth Matrix; (e) rows corresponding to the maximum value in the Polarization Angle-Depth Matrix  
图5 三种场景下的极化角度-深度矩阵仿真结果:(a) 携带手雷模型;(b) 携带手枪模型;(c) 未携带武器;(d) 极化角度-深度矩阵的第一列;(e) 极化角度-深度矩阵最大值所在的行

In the polarization angle dimension, weapon-bearing individuals exhibit higher amplitude values, while their phase characteristics vary depending on weapon types and rotation angles. In the depth dimension, multiple peaks emerge in the depth spectrum of armed individuals due to multiple scattering from concealed weapons, with higher peak values resulting from the superior scattering coefficients of metallic materials. These distinct features enable effective differentiation between individuals with and without concealed weapons.

Notably, the Polarization Angle-Depth Matrix also differs between grenade-carriers and handgun-bearers. Grenade carriers demonstrate significantly higher amplitudes and more numerous depth spectrum peaks. This discrepancy originates from the cross-polarization echo power basis of the Polarization Angle-Depth Matrix. Under the linear polarization wave incidence, cross-polar-

ization components primarily derive from multiple scatterings. The cylindrical geometry of grenades promotes enhanced multiple scattering interactions within paired grenade configurations, thereby enhancing cross-polarization power and generating additional peaks. Conversely, handgun surfaces predominantly exhibit planar structures facing transceiver antennas, resulting in weaker cross-polarization components with consequently lower amplitudes and fewer peaks. Furthermore, grenade models possess larger cross-sections than handguns, receiving stronger incident power from transmitting antennas and therefore producing higher-power scattered echoes.

## 2.2 Experimental results

We conducted experiments using a self-built experimental platform and a dummy model. The transmitting and receiving antennas were each fixed on two perpendicular rotary stages, allowing for the adjustment of the polarization angle via the rotation of the stages. In the experiments, grenade and metallic handgun models were selected as target objects. The measurement equipment included a vector network analyzer (VNA) and frequency extension modules, covering a frequency range of 75-110 GHz with a frequency step size of 0.175 GHz, where signals were generated via discrete frequency-stepped point-by-point scanning. The polarization angle range was set from  $0^\circ$  to  $180^\circ$ , with a sampling interval of  $10^\circ$ . The distance between the dummy and the antennas was 1.2 meters. The experimental platform as well as the weapons and clothing used in the experiment are shown in Fig. 6.

It is important to note that in the experiment, the

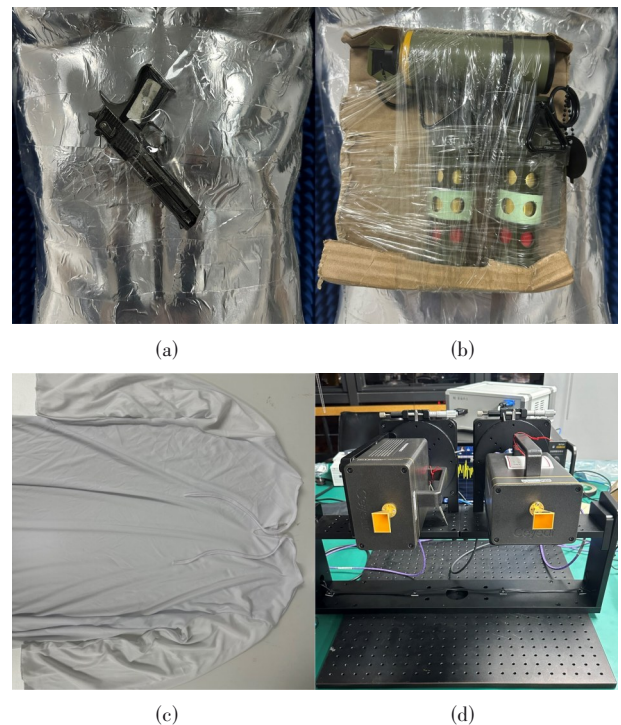


Fig. 6 Photos of the experimental scenario: (a) handgun model; (b) grenade model; (c) clothing; (d) experimental platform  
图6 实验场景照片:(a) 手枪模型;(b) 手雷模型;(c) 覆盖衣物;(d) 实验平台

transmitting and receiving antennas were placed side by side, rather than using a beam splitter to simulate a quasi-monostatic configuration. This was because the experiment only required power information and did not need phase information. By placing the two antennas in parallel, coupling between the transmitter and receiver was reduced, simplifying the experimental design and improving measurement stability.

The Polarization Angle-Depth Matrix obtained from the experiment is shown in Fig. 7, where the cross-polarization echo power has been normalized according to the frequency response of the transmitted power.

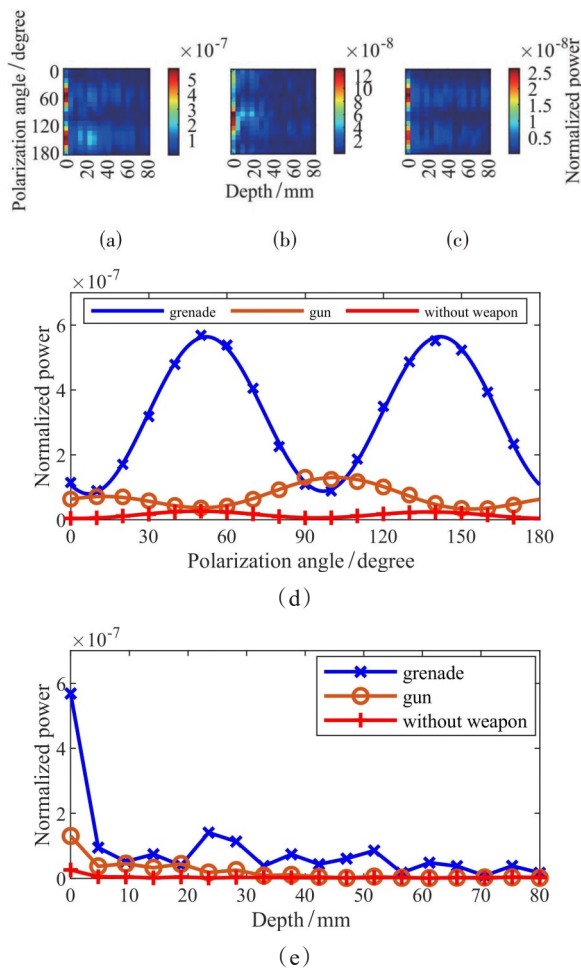


Fig. 7 Experimental results of the Polarization Angle-Depth Matrix in three scenarios: (a) carrying grenade model; (b) carrying handgun model; (c) without weapons; (d) first column of the Polarization Angle-Depth Matrix; (e) rows corresponding to the maximum value in the Polarization Angle-Depth Matrix

图7 三种场景下的极化角度-深度矩阵实验结果:(a)携带手雷模型;(b)携带手枪模型;(c)未携带武器;(d)极化角度-深度矩阵的第一列;(e)极化角度-深度矩阵最大值所在的行

Compared with the simulation results in Fig. 5, the experimental results presented in Fig. 7 exhibit discrepancies in detail, primarily attributed to simulation modeling errors and environmental interference. For instance, in Fig. 7(d), the peak position in the handgun model's fitting results deviates from Fig. 5(d), mainly due to

variations in handgun rotation angles. Similarly, the depth spectrum peaks of grenades in Fig. 7(e) differ from those in Fig. 5(e), caused by discrepancies between simulated and actual grenade geometries.

Nevertheless, experimental results of the Polarization Angle-Depth Matrix between armed and unarmed individuals exhibit statistically significant differences in both polarization angle and depth dimensions, including amplitude, peak distribution patterns, and peak values, which demonstrate consistency with simulation-derived statistical characteristics. These results indicate that the Polarization Angle-Depth Matrix can effectively characterize the differences in polarization response and depth distribution between individuals carrying weapons and normal individuals. This validates its potential application for concealed weapon detection.

### 3 Conclusion

This study introduces the Polarization Angle-Depth Matrix by scanning the incident polarization angle and capturing multiple depth spectrums in millimeter-wave direct detection. Through the theoretical analysis of the variation of cross-polarization power with the incident polarization angle and the depth spectrum representation of multi-layer medium, it is observed that the human body surface and concealed weapons exhibit significant differences in polarization response and depth distribution. Simulation and experimental results validate that these features exhibit strong potential for detecting concealed weapons on individuals, highlighting its applicability in human security screening.

### References

- [1] Wang Z, Chang T, Cui H L. Review of active millimeter wave imaging techniques for personnel security screening [J]. *IEEE Access*, 2019, 7: 148336 - 148350.
- [2] Liu X, Yang J, Li W, et al. Tightly coupled modeling and reliable fusion strategy for polarization-based attitude and heading reference system [J]. *IEEE Transactions on Industrial Informatics*, 2023, 19 (1): 62 - 73.
- [3] Hu P, Yang J, Qiao J, et al. Underwater downwelling radiance fields enable three-dimensional attitude and heading determination [J]. *IEEE Transactions on Industrial Informatics*, 2024, 20(2): 2109 - 2118.
- [4] Salmon N A. Indoor full-body security screening: Radiometric microwave imaging phenomenology and polarimetric scene simulation [J]. *IEEE Access*, 2020, 8: 144621 - 144637.
- [5] Cheng Y, Wang Y, Niu Y, et al. Regional-based object detection using polarization and fisher vectors in passive millimeter-wave imaging [J]. *IEEE Transactions on Microwave Theory and Techniques*, 2023, 71(5): 2702 - 2713.
- [6] Tedeschi J, Bernacki B, Sheen D, et al. Fully polarimetric passive W-band millimeter wave imager for wide area search [C]. *Proceedings of SPIE 8873, Polarization Science and Remote Sensing VI*, 2013: 88730V-1 - 88730V-14.
- [7] Kim W G, Moon N W, Kim H K, et al. Linear polarization sum imaging in passive millimeter-wave imaging system for target recognition [J]. *Progress in Electromagnetics Research*, 2013, 136: 175 - 193.
- [8] Cheng Y, Wang Y, Niu Y, et al. Physically based object contour edge display using adjustable linear polarization ratio for passive millimeter-wave security imaging [J]. *IEEE Transactions on Geoscience and Remote Sensing*, 2021, 59(4): 3177 - 3191.
- [9] Cheng Y, Wang Y, Niu Y, et al. Concealed object enhancement using multi-polarization information for passive millimeter and terahertz wave security screening [J]. *Optics Express*, 2020, 28(4):

- 6350 - 6366.
- [10] Li N, Zhao Y, Pan Q, et al. Removal of reflections in LWIR image with polarization characteristics[J]. *Optics Express*, 2018, 26(12): 16488 - 16504.
- [11] Cheng Y, You Y, Zhu D, et al. Reflection removal using dual-polarization and saliency in millimeter-wave and terahertz imaging [J]. *IEEE Transactions on Geoscience and Remote Sensing*, 2021, 59(10): 9439 - 9447.
- [12] McMakin D L, Sheen D M, Griffin J W, et al. Extremely high-frequency holographic radar imaging of personnel and mail [C]. *Proceedings of SPIE 6201, Sensors and Command, Control, Communications, and Intelligence (C3I) Technologies for Homeland Security and Homeland Defense V*, 2006: 62011W-1 - 62011W-6.
- [13] Harmer S, Bowring N, Andrews D, et al. A review of nonimaging stand-off concealed threat detection with millimeter-wave radar[J]. *IEEE Microwave Magazine*, 2012, 13(1): 160 - 167.
- [14] Andrews D A, Harmer S W, Bowring N J, et al. Active millimeter wave sensor for standoff concealed threat detection[J]. *IEEE Sensors Journal*, 2013, 13(11): 4948 - 4954.
- [15] Harmer S W, Bowring N J, Rezgui N D, et al. A comparison of ultra wideband conventional and direct detection radar for concealed human carried explosives detection [J]. *Progress in Electromagnetics Research Letters*, 2013, 39: 37 - 47.
- [16] Harmer S W, Bowring N, Andrews D, et al. Millimeter radar threat level evaluation (MiRTLE) at standoff ranges [C]. *Proceedings of SPIE 8188, Millimeter Wave and Terahertz Sensors and Technology IV*, 2011: 81880L-1.
- [17] Zhang L, Cheng Y, Li S, et al. Dual-polarized anomaly detection system based on millimeter-wave lens antenna [C]. *2024 IEEE International Symposium on Antennas and Propagation and INC/USNC-URSI Radio Science Meeting (AP-S/INC-USNC-URSI)*, 2024: 881 - 882.
- [18] Adametz J, Schmidt L P. Threat object classification with a close range polarimetric imaging system by means of H-alpha decomposition [C]. *2013 European Radar Conference*, 2013: 77 - 80.
- [19] Migliaccio C, Brochier L, Lanteri J, et al. MMW imaging using polarimetric measurements [C]. *2019 16th European Radar Conference (EuRAD)*, 2019: 265 - 268.
- [20] Robertson D A, MacFarlane D G, Cassidy S L, et al. Submillimeter wave 3D imaging radar for security applications [C]. *IET Colloquium on Millimeter-Wave and Terahertz Engineering and Technology 2016*, 2016: 1 - 5.
- [21] Robertson D A, Macfarlane D G, Hunter R I, et al. The CONSORTIS 16-channel 340-GHz security imaging radar [C]. *Proceedings of SPIE 10634, Passive and Active Millimeter-Wave Imaging XXI*, 2018: 58 - 67.
- [22] Robertson D A, Macfarlane D G, Hunter R I, et al. A high frame rate, 340 GHz 3D imaging radar for security [C]. *2018 IEEE Radar Conference (RadarConf18)*, 2018: 55 - 60.
- [23] Gorman J, Douglass R, Burns T. System and method for standoff detection of human carried explosives: U.S. Patent 6,967,612 [P]. 2005-11-22.